nature communications

Article

https://doi.org/10.1038/s41467-025-68068-7

Unconventional polaronic ground state in superconducting $LiTi_2O_4$

Received: 3 January 2025

Accepted: 16 December 2025

Published online: 06 January 2026

Check for updates

Zubia Hasan[1,16], Grace A. Pan[1,16], Harrison LaBollita[2], Austin Kaczmarek[3], Suk Hyun Sung[4], Shekhar Sharma[2], Purnima P. Balakrishnan[5], Edward Mercer[6,7], Vivek Bhartiya[8], Alpha T. N'Diaye[9], Zaher Salman[10], Thomas Prokscha[10], Andreas Suter[10], Alexander J. Grutter[5], Mirian Garcia-Fernandez[11], Ke-Jin Zhou[11], Jonathan Pelliciari[8], Valentina Bisogni[8], Ismail El Baggari[4], Darrell G. Schlom[12,13,14,15], Matthew R. Barone[12], Charles M. Brooks[1], Katja C. Nowack[3], Antia S. Botana[2], Brendan D. Faeth[12], Alberto de la Torre[6,7] ✉ & Julia A. Mundy[1] ✉

Geometrically frustrated lattices can display a range of correlated phenomena, ranging from spin frustration and charge order to dispersionless flat bands due to quantum interference. One particularly compelling family of such materials is the half-valence spinel LiB_2O_4 materials. On the *B*-site frustrated pyrochlore sublattice, the interplay of correlated metallic behavior and charge frustration leads to a superconducting state in $LiTi_2O_4$ and heavy fermion behavior in LiV_2O_4. To date, however, $LiTi_2O_4$ has primarily been understood as a conventional BCS superconductor despite a lattice structure that could host more exotic ground states. Here, we present a multimodal investigation of $LiTi_2O_4$, combining ARPES, RIXS, proximate magnetic probes, and ab-initio many-body theoretical calculations. Our data reveals a novel mobile polaronic ground state with spectroscopic signatures that underlie co-dominant electron-phonon coupling and electron-electron correlations also found in the lightly doped cuprates. The cooperation between the two interaction scales distinguishes $LiTi_2O_4$ from other superconducting titanates, suggesting an unconventional origin to superconductivity in $LiTi_2O_4$. Our work deepens our understanding of the rare interplay of electron-electron correlations and electron-phonon coupling in unconventional superconducting systems. In particular, our work identifies the geometrically frustrated, mixed-valence spinel family as an underexplored platform for discovering unconventional, correlated ground states.

The interplay between electron–electron correlations and electron–phonon coupling has been of long-standing interest in understanding superconductivity. In traditional Bardeen-Cooper-Schrieffer (BCS) superconductors, Coulomb repulsion between electrons is thought to screen electron-phonon coupling and reduce the superconducting transition temperature T_c[1]. In unconventional superconductors, however, there can be a more complex interplay between electron–phonon coupling and electron–electron interactions. Strong correlations can further strengthen the electron-phonon coupling and enhance T_c[2–4]. In certain cases, as explored for cuprates[5], the energy scales of strong electron–electron correlations can overwhelm those of electron–phonon interactions, leading to charge and spin fluctuations that compete with or enhance superconductivity[6]. Thus, understanding how electronic correlations and electron–phonon coupling interact in

A full list of affiliations appears at the end of the paper. ✉e-mail: a.delatorreduran@northeastern.edu; mundy@fas.harvard.edu

https://doi.org/10.1038/s41467-025-68068-7

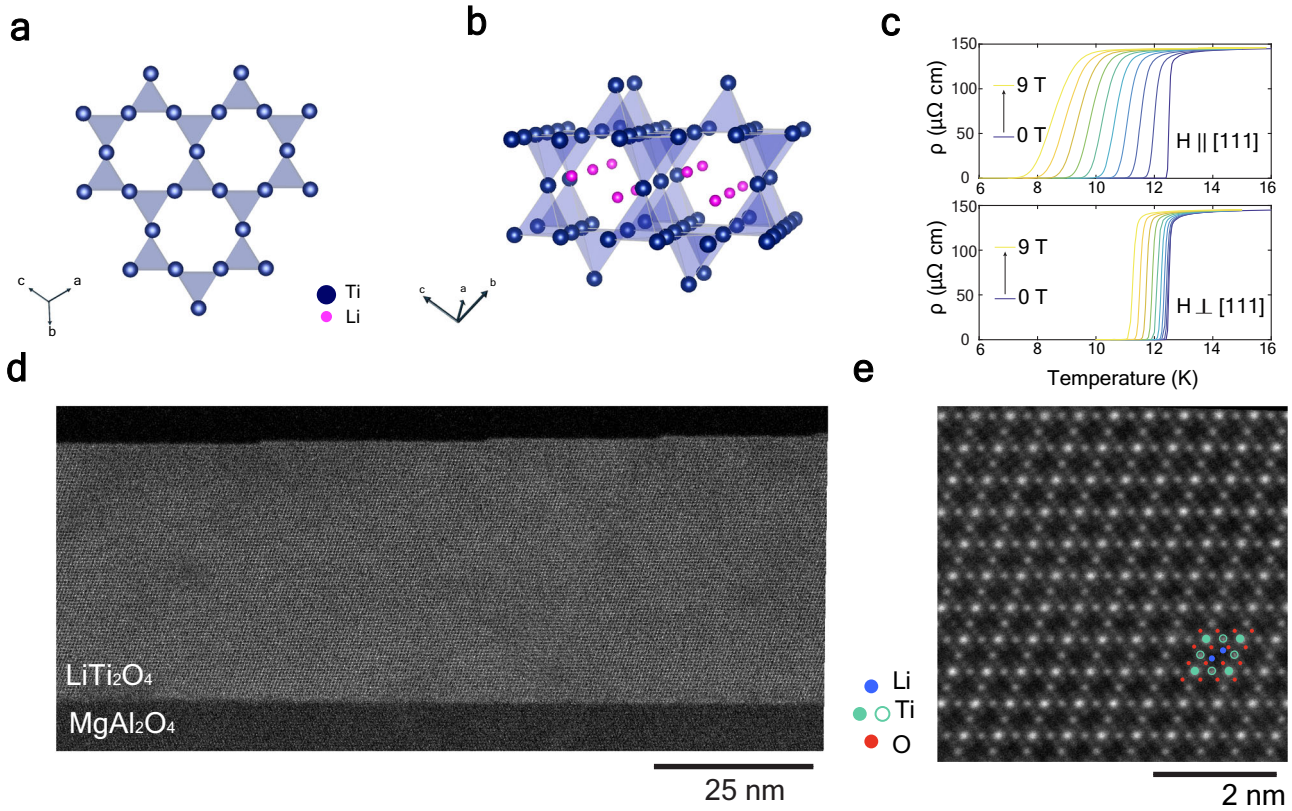

Fig. 1 | Structural and electrical characterization of $LiTi_2O_4$. a The (111) plane of $LiTi_2O_4$ showing the titanium kagome sublattice inherent to the spinel structure. **b** Side-view of the (111) plane shown in **a**, highlighting the three-dimensional nature of the geometric frustration in $LiTi_2O_4$. **c** Resistivity ρ vs temperature of $LiTi_2O_4$ with magnetic field (0 to 9 T) parallel and perpendicular to the sample. **d** Large field-of-view HAADF-STEM image of $LiTi_2O_4$ showing uniform crystallinity over a large area. **e** Local HAADF-STEM image of $LiTi_2O_4$ overlaid with the corresponding atoms.

superconductors is important in identifying new families of unconventional superconductors and ascertaining the mechanisms behind high-temperature superconductivity.

Although superconductivity was discovered in $LiTi_2O_4$ before the cuprates[7], it remains a unique instance of a spinel superconductor and with the highest T_c for a mixed-valence titanate. In this crystal structure, $d^{0.5}$ titanium atoms form a pyrochlore sublattice, composed of alternating planes of Kagome and triangles (Fig. 1a, b). While this geometric construction has given rise to strong electron correlations in other systems[8], these interactions have been largely unexplored in $LiTi_2O_4$. Indeed, superconductivity in $LiTi_2O_4$ has primarily been considered as phonon-mediated BCS-like, supported by specific heat, tunneling spectroscopy, and muon spin rotation measurements[9–11]. In contrast, anomalous magnetotransport behavior and scanning tunneling spectroscopy experiments have suggested the presence of spin fluctuations, orbital ordering, and pseudo-gap-like states in $LiTi_2O_4$, all of which are typically associated with unconventional superconductors and strongly correlated materials[10,12,13]. Interestingly, previous theoretical studies of $LiTi_2O_4$ have suggested non-BCS-like superconducting mechanisms, such as bipolaronic[14,15] or resonating valence bond (RVB) superconductivity[16,17]. While there have been speculations about the role of electron–electron correlations[9,18], a more detailed investigation into the strength and nature of various correlations is needed to explore the notion of "unconventional superconductivity" in $LiTi_2O_4$.

Here, we reveal the complex interplay between electron–phonon coupling and electron–electron interactions in $LiTi_2O_4$. We use molecular-beam epitaxy (MBE) to synthesize epitaxial thin films of superconducting $LiTi_2O_4$, enabling a detailed spectroscopic investigation using resonant inelastic x-ray scattering (RIXS) and angle-resolved photoemission spectroscopy (ARPES). The combination of the element-specific sensitivity to structural and local excitations of RIXS, together with the unique capability of ARPES to reveal energy and momentum dependence of the quasiparticle self-energy, enables us to provide a comprehensive description of the low-energy physics of $LiTi_2O_4$. We observe evidence of strong electronic correlations and signatures of strong electron–phonon coupling. The cooperation between these two interaction scales gives rise to a novel polaronic ground state—also found in weakly doped cuprates[19]—that dynamically localizes titanium states in $LiTi_2O_4$. This interpretation is further supported by our theoretical calculations, which can reproduce some of the spectral features in our ARPES data when considering electron correlations or electron–phonon interactions separately, but are unable to reproduce polaronic phenomena associated with the interplay of both interactions. Our work thus challenges the notion of phonon-dominated BCS superconductivity in $LiTi_2O_4$ by revealing the complex correlations present in this material, hearkening comparisons to cuprate-like physics.

Results

Synthesis and characterization of superconducting $LiTi_2O_4$

Thin films of $LiTi_2O_4$ were grown via reactive oxide MBE on (111)-oriented $MgAl_2O_4$ substrates (see "Methods"). As shown in Fig. 1c, the films display a superconducting transition with T_c ~ 12.5 K and a residual resistivity ratio (RRR) of ~ 5.85 (Fig. S3), consistent with previous reports of the highest quality $LiTi_2O_4$[7,10]. Figure 1d, e show high-angle annular dark field scanning transmission electron microscopy (HAADF-STEM) images of $LiTi_2O_4$, attesting to the high structural quality of our films (also see Supplementary Fig. S1).

Additionally, we confirm the onset of superconductivity and probe the superconducting order parameter using scanning

https://doi.org/10.1038/s41467-025-68068-7

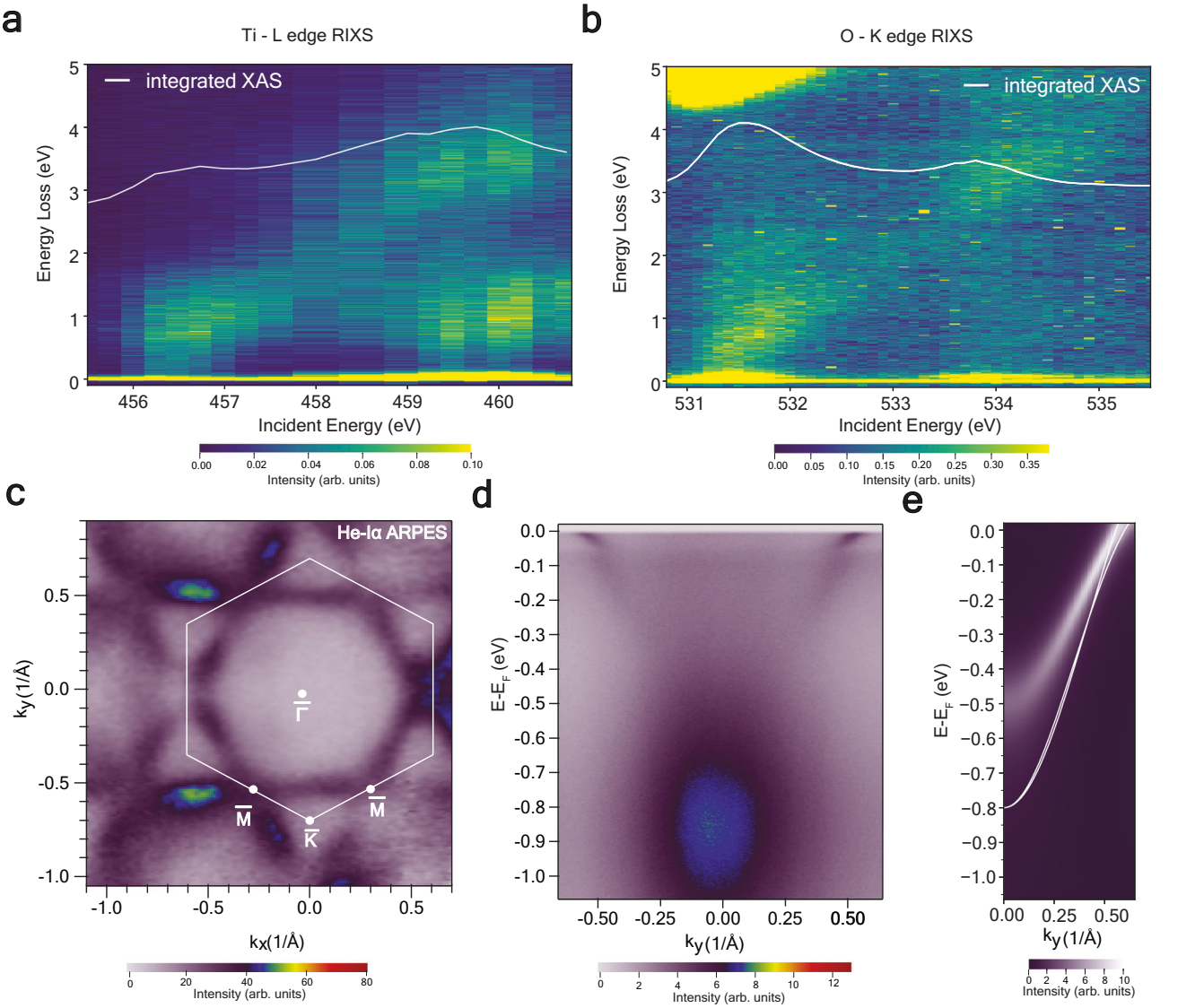

Fig. 2 | Electron–electron correlations in $LiTi_2O_4$. **a** RIXS intensity at the Ti-L_3 edge. **b** RIXS intensity at the O K-edge. **c** Iso-energy map at the Fermi level taken with He-Iα showing a hexagonal Fermi surface. The white hexagon indicates the first Brillouin zone. **d** Experimental band structure in the $\bar{K} - \bar{\Gamma} - \bar{K}$ direction. **e** DMFT and DFT (white) comparison along $\bar{\Gamma} - \bar{K}$ indicating the mass renormalization due to electron–electron correlations.

superconducting quantum interference device (SQUID) microscopy, which locally measures magnetic susceptibility (Fig. S4). The measured magnetic susceptibility can be used to extract the temperature dependence of the reduced London penetration depth (Supplementary Material Section S3), which can be well-fit by a fully gapped order parameter, consistent with *s*-wave-like pairing. The observation of the 2-D thin film limit of superconductivity, the high RRR, as well as a homogeneous diamagnetic response from scanning SQUID, demonstrates the high structural quality of our films, ensuring that further measurements probe the intrinsic behavior of $LiTi_2O_4$.

Electron–electron correlations in $LiTi_2O_4$

Poised with high-quality thin films, we first probe the electronic structure using elemental-specific RIXS measurements. Figure 2a shows the RIXS intensity of $LiTi_2O_4$ near the Ti-L_3 edge. Our x-ray absorption spectroscopy (XAS) data (Fig. S16a) display resonant features associated with the mixed valence Ti^{4+} and Ti^{3+} states (for a detailed discussion on the mixed-valence XAS, see Supplementary Section S9). Given the lack of *dd* excitations expected for a trivial d^0 state, we conclude that the broad Raman-like *dd* features centered at $E_{loss} = 1.5$ eV and $E_{loss} = 4$ eV, reflect a d^1 titanium occupation state, which, given the lack of charge order in $LiTi_2O_4$, can only be dynamically populated[20]. These Raman-like excitations, along with the suppressed fluorescence contribution, are unexpected, given that the itinerant charge carriers in our metallic and superconducting samples are proposed to have a dominant Ti-3*d* band character near the Fermi level[21,22]. We note that our RIXS data resemble that of $MgTi_2O_4$[23] despite $LiTi_2O_4$ lacking large static local trigonal distortions of the TiO_6 octahedra and Ti-Ti dimerization (Supplementary Figs. S1 and S22). The qualitative similarities between the RIXS energy maps in metallic $LiTi_2O_4$ and Mott-insulating systems like $MgTi_2O_4$ are suggestive of the presence of localized excitations in $LiTi_2O_4$.

In addition to the Raman-like excitations, we observe spectral weight associated with a fluorescence contribution with a linear dispersion in E_i that extends below $E_{loss} \leq 1.5$ eV. This resembles the superposition of localized and delocalized excitations observed in negative charge transfer insulators[24]. Moreover, O K-edge RIXS, shown in Fig. 2b, also shows Raman-like and fluorescence contributions below the charge transfer gap, $\Delta \approx 4.5$ eV. This is the same energy as the intra-*dd* excitations at the Ti L_3-edge, suggesting strong hybridization

https://doi.org/10.1038/s41467-025-68068-7

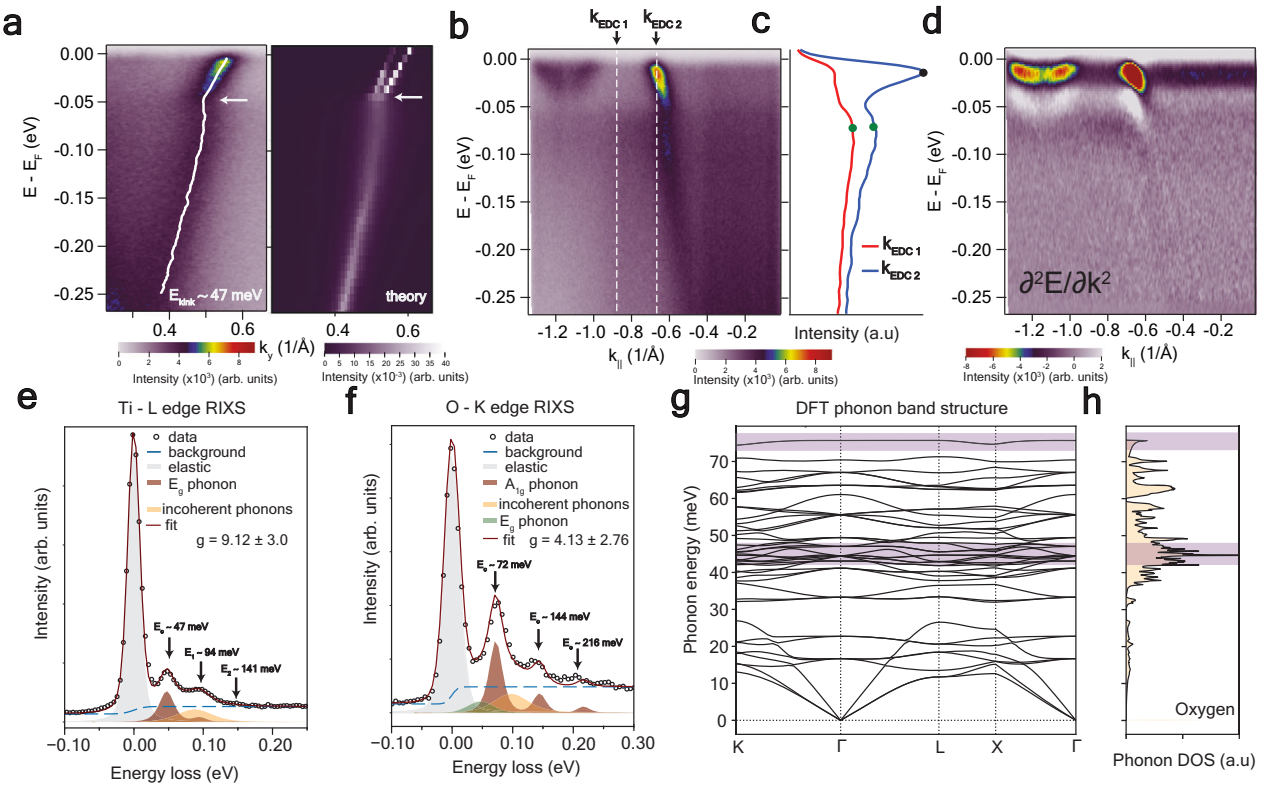

Fig. 3 | Electron–phonon coupling in $LiTi_2O_4$. **a** Comparison of the $\bar{\Gamma}-\bar{K}$ ARPES data to density-functional perturbation theory (DFPT) highlighting the kink feature at 47 meV at $\bar{\Gamma}-\bar{K}$ at $T = 7$ K. **b** Energy - momentum ARPES spectra along the $\bar{\Gamma}-\bar{K}-\bar{M}$ direction. **c** EDC cuts at two different $k_{||}$ highlighted in (**b**) with dotted white lines. Black and green dots correspond to the top of the two EDC poles. **d** Second-derivative plot from (**b**) highlighting a dispersionless spectral intensity at the second pole denoted by a black arrow in (**c**) also observable in the raw data in (**b**). A spectral gap is also prominent at the same energy scale where the dispersionless feature interrupts the main band. **e** Quasi-elastic RIXS excitations shown at $E_{inc} = 460$ eV for the Ti-L_3 edge. **f** Quasi-elastic RIXS excitations shown at $E_{inc} = 531.5$ eV for the O K-edge. The total intensity is a fit (red solid line) to a Voigt peak (gray shading), a background step function (blue dashed lines), one (two) Gaussian(s) and an Ament model fit to the phonon spectra (maroon) in (**e**), (**f**), respectively. **g**, **h** Calculated phonon band structure and total oxygen phonon density of states, respectively. The purple box highlights the energy scale of the A_{1g} and E_g modes, respectively, in both plots.

between titanium and oxygen carriers. While the hybridization between Ti-3*d* and O-2*p* states has been previously theorized[21], the RIXS data is the first instance of direct observation of strong titanium-oxygen hybridization. Moreover, the presence of fluorescence contributions at the O-*K*-edge near the elastic line (zero energy loss) suggests a larger contribution of oxygen carriers to electronic transport in $LiTi_2O_4$ than that expected from previous density of states calculations[21]. Thus, our RIXS data suggest the presence of charge localization, Ti-3*d* and O-2*p* hybridization, and electron–electron correlations in $LiTi_2O_4$.

Electron–electron correlations are also observed in in-situ ARPES measurements on $LiTi_2O_4$. Figure 2c shows the Fermi surface of $LiTi_2O_4$ from our ARPES measurements. Here, k_x and k_y are chosen to lie along the $[11\bar{2}]$ and $[\bar{1}10]$ directions, respectively. The Fermi surface is characterized by large electron pockets with hexagonal symmetry centered at Γ, pushing toward the zone boundary in proximity to a Lifshitz transition, which has led to enhanced electronic interactions near the Fermi surface for other superconductors[25]. A more detailed discussion of the Fermi surface and its k_z dependence is given in Supplementary Figs. S5, S6 and in the Supplementary Material Section S4.

To analyze the electronic interactions, we look at high-symmetry cuts of the band structure of $LiTi_2O_4$. In Fig. 2d, e, we compare our experimental band structure along $\bar{\Gamma}-\bar{K}$ to the momentum-resolved spectral function obtained from density-functional theory plus dynamical mean-field theory (DFT+DMFT). The non-interacting band dispersion is shown in white in Fig. 2e for reference. The DFT+DMFT calculation reproduces the experimental dispersion near Γ, capturing the large effective mass renormalization compared to the bare DFT band—a clear indication of strong electron correlations in $LiTi_2O_4$. The calculated cyclotron mass (Supplementary Material Fig. S9) yields $\frac{m_{eff}}{m_{bare}} = 2.53 \pm 0.4$. This method of calculating the renormalization agrees with previous reports of the effective mass of $LiTi_2O_4$ by other optical probes[26,27]. Additionally, we observe a broad Gaussian-like, intense incoherent spectral weight centered at $E_B \approx 0.9$ eV that resembles the lower Hubbard band of lightly doped cuprates[28]. Similar to the cuprates, the spectral weight shows k_z dependence with a transition from a "champagne glass-like dispersion" to a "waterfall" feature[29] in the data taken by Ne-Iα photon energy (16.85 eV) (Supplementary Fig. S6b). We note this feature cannot be reproduced by DMFT calculations but is consistent with a previous photoemission spectroscopy measurement of $LiTi_2O_4$, where it was interpreted as a signature of polaronic behavior[14]. Nonetheless, our combined ARPES and RIXS data provide the first observation of significant electronic correlations in $LiTi_2O_4$.

Electron–phonon coupling in $LiTi_2O_4$

While electronic correlations play a key role in unconventional superconductivity, we also observe signatures of electron–phonon coupling in the electronic structure of $LiTi_2O_4$. Consistent with previous ARPES reports[30], we observe a "kink" at $E_B \approx 46$ meV as shown in Fig. 3a. This feature is ascribed to an E_g oxygen phonon mode by tunneling spectroscopy measurements[31] and inelastic neutron scattering[32], confirmed by calculations of the spectral function including the self-energy from only electron–phonon interactions

(Supplementary Material Section S5). We extract a band renormalization, $\lambda_{tot} = 1.80(1)$, three times higher than $\lambda_{e-ph} = 0.65$ determined by specific heat measurements[9] and ab-initio calculations[18]. The extracted band renormalization value from our ARPES data is comparable to that from electronic specific heat measurements, where the larger value is attributed to enhancement from electron–electron correlations or spin fluctuations[22,33,34]. We note that λ_{tot} includes λ_{e-ph} as well as λ_{e-e}. While a precise determination of just λ_{e-ph} is non-trivial due to the interlinked nature of electron–electron correlations and electron–phonon coupling in this compound, we can approximate $\lambda_{e-ph} \approx 1.3 \pm 0.5$ by fitting the dispersion of the band at lower binding energies as the bare band, consistent with λ_{e-ph} extracted from other ARPES measurements on this compound[30]. For a more detailed discussion on the calculation of λ_{tot} and λ_{e-ph} as well as their temperature and momentum dependence, see Supplementary Material Section S4 and Fig. S7.

Figure 3b shows an energy-momentum cut along the $\bar{\Gamma} - \bar{K} - \bar{M}$ direction (cut overlaid on the Brillouin zone is shown in Fig. S8a). Here we observe a non-dispersive feature at $E_B = 70.4 \pm 6$ meV at all $k_{||}$, highlighting the accumulation of incoherent spectral weight below the main kink at $E = 46$ meV (Fig. 3a). To examine this flat feature, we present two energy dispersive cuts (EDC) in Fig. 3c, k_{EDC1} which cuts across momentum value devoid of bands and k_{EDC2} which cuts across the k_F of the main $LiTi_2O_4$ band. The momentum position of these two cuts is indicated by two black arrows pointing to dotted white lines in Fig. 3b. We can see the peak position of this sub-band in the EDC of k_{EDC1} as an abrupt and sharp increase in spectral intensity at $\Omega = 70.4 \pm 6$ meV (green dot), also observed in k_{EDC2} at the same energy scale. Sub-bands like these are indicative of a highly interacting picture[35], in stark contrast to a non-interacting picture, where, in the absence of any bands, the expected EDC would not have any additional poles, unlike what is seen in k_{EDC1}. The second derivative plot (Fig. 3d) further highlights this feature and additionally shows a “spectral gap" where the non-dispersive feature interrupts the main dispersive electronic band. We note that the flat feature, in addition to the spectral gap, can also be seen clearly in our raw data in Fig. 2d. These types of sub-bands due to strong electron-phonon coupling are spectral signatures that are consistent with the formation of intra-unit cell small polarons[36] that have been observed in other correlated materials[35,37].

Our RIXS measurements also corroborate the presence of strong electron-phonon coupling and multiphonon processes in $LiTi_2O_4$. Figure 3e shows the RIXS spectra at the Ti L_3- and O K-edges, respectively. As highlighted by black arrows in Fig. 3e, f, both RIXS spectra are characterized by prominent quasi-elastic peaks that are approximately equally spaced and monotonically decay with E_{loss}, thus resembling the harmonic progression of the multiphononic processes. The low-energy excitations shown in the titanium spectra are well fit by the Ament model[38], which considers a single non-dispersive phonon mode coupled to the electronic structure with strength g (See Supplementary Material Section S6 for more details on the Ament model fit). At the Ti-L_3 edge, the Ament model in conjunction with a broad Gaussian peak centered at $E_{loss} = 90$ meV provides a good fit for a mode centered at $\Omega = 47 \pm 2$ meV, in agreement with the oxygen E_g mode observed in ARPES. We interpret this broad Gaussian peak to represent multiple incoherent phononic excitations that cannot be resolved within the energy resolution of the instrument, also observed in $MgTi_2O_4$[23].

The coupling strength, $g_{Ti} = 9.1 \pm 3.0$, far exceeds those of other titanates[39,40], and is on par with some cuprates measured via RIXS[41] further supporting strong electron-phonon coupling in $LiTi_2O_4$. Moreover, the observation of a pure oxygen E_g mode at the titanium edge is indicative of strong hybridization between the O-2p and the Ti-3d orbitals. Similar to the Ti L_3-edge, the three excitations at the O K-edge can also be well fit by the Ament model in conjunction with two broad Gaussian peaks. The fit gives us the first three harmonics of a phonon mode centered at $\Omega = 72 \pm 1$ meV with $g_O = 4.13 \pm 2.76$. We assign this mode to the oxygen A_{1g} phonon, which is known to be strongly coupled to the E_g mode[18]. While the A_{1g} mode is coherent at the O K-edge, the broad Gaussian centered at $E \approx 46$ meV, which encodes the coupling to the E_g mode also seen at the Ti L-edge, indicates a reduced coherence of this mode at the O K-edge. The absence of higher harmonics of the E_g mode at the O K-edge might be due to the higher density of oxygen modes at that energy, as shown in Fig. 3h (For a detailed discussion on the different phonon modes, see Supplementary Section 6). We note that our DFT calculations of the phonon band structure (Fig. 3g) show the modes around $\Omega \approx 46$ meV and ≈ 75 meV to be relatively nondispersive, supporting our choice of Ament model fitting for the quasi-elastic peaks at the Ti L_3- and O K-edges.

Discussion

Our combined spectroscopic data indicate that the effects of electron–electron correlations and electron-phonon coupling cannot be disentangled in $LiTi_2O_4$. Moreover, ab-initio calculations (Figs. 2e and 3a) treating electron-phonon coupling and electron–electron correlations separately fail to capture the most salient features of our data, namely the existence of localized excitations in $LiTi_2O_4$ (Fig. 2a) and the presence of a second pole in the photoemission self-energy (Fig. 3c). While the combined theoretical description of these two energy scales remains challenging and a matter of active research[42], there is growing evidence that the excitation spectrum, band structure and transport properties of quantum materials such as $SrVO_3$[43] and superconductors like alkalli-fullerides[37] and the cuprates[44] can only by understood through the interplay of both interaction scales. We note that while competing interactions are generally associated with unconventional superconductivity, our scanning SQUID data are consistent with a conventional s-wave order parameter (Supplementary Section S3). This naturally also raises the question as to how the phonon-mediated attractive interaction—essential for s-wave superconductivity—is robust against or potentially enhanced by the repulsive electronic correlations apparent in $LiTi_2O_4$. Within this context, $LiTi_2O_4$ departs from $SrTiO_3$[45] and other superconducting titanates[46,47] where electron-phonon coupling is understood to be the dominant interaction.

We finally comment on the possible mechanism that enables the strong interplay of electron–electron and electron-phonon interactions in $LiTi_2O_4$. In this context, it is instructive to consider the $d^{0.5}$ occupation state in $LiTi_2O_4$ in the context of the d^1 member of the AB_2O_4 family, $MgTi_2O_4$. In $MgTi_2O_4$, a trigonal distortion driven by E_g and A_{1g} oxygen phonons[48] lifts the orbital degeneracy of the Ti $3d^1$ state in a perfect cubic octahedral environment (Fig. 4a, b). The combination of this local distortion with the formation of Ti-Ti dimers at $T = 260$ K[48] leads to a tetragonal, dimerized unit cell and the formation of a correlated insulating state (Fig. 4b) in $MgTi_2O_4$. In the $d^{0.5}$ mixed-valence state, the energy gain from dimerization is reduced in favor of a charge-ordered ground state, such as in mixed-valence spinel $CuIr_2S_4$[49]. However, no static symmetry breaking due to orbital or lattice ordering has been reported in $LiTi_2O_4$[10], possibly due to the geometric frustration inherent in the spinel structure. This raises the question of how the d^1 state, with its associated local distortion, is accommodated in $LiTi_2O_4$. We speculate that in $LiTi_2O_4$ with an occupation $d^{0.5}$ in the absence of charge order, two titanium ions share an electron dynamically, such that their occupation state fluctuates between d^1 and d^0. In this scenario, the transiently occupied d^1 site has an associated local symmetry reduction due to dynamic lattice fluctuations of the E_g and A_{1g} oxygen phonons, as seen in $MgTi_2O_4$[50]. As the electron moves to the unoccupied d^0 site, it drags the local distortion with it, leading to the formation of a polaronic state in which charge motion and lattice distortions are coupled (Fig. 4b). Notably, this polaronic mechanism for Ti^{3+} defect induced carriers in a Ti^{4+} system has already been proposed for $Li_4Ti_5O_{12}$[51], suggesting a similar

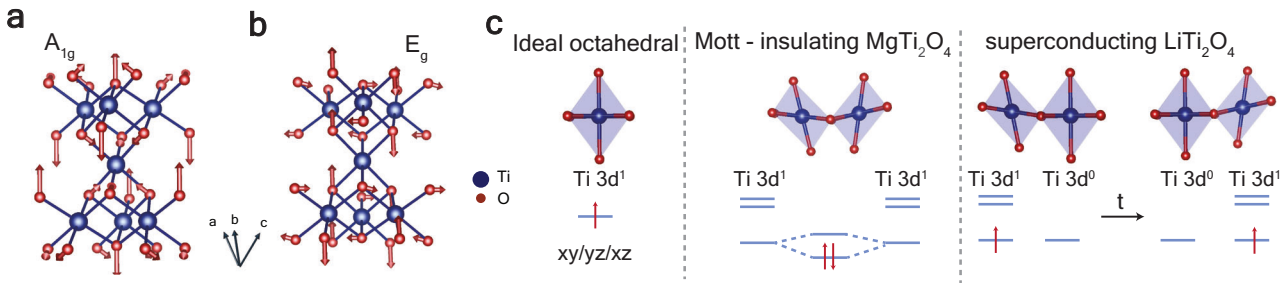

Fig. 4 | Polaron formation in $LiTi_2O_4$. a, b DFT calculated A_{1g} and E_g oxygen phonon modes in $LiTi_2O_4$. **c** An ideal TiO_6 octahedra (left) with a highly degenerate d^1 state in a cubic crystal field. In $MgTi_2O_4$, a local trigonal distortion driven by E_g and A_{1g} phonons is required to achieve a dimerized ground state (middle). Dynamic symmetry-reducing local lattice fluctuations associated with electron hopping leading to polaron formation in $LiTi_2O_4$ (right).

mechanism for polaronic transport in $LiTi_2O_4$ where the mixed-valence is native to the material.

Our data reflect the formation of such a small mobile polaronic state in $LiTi_2O_4$. First, our ARPES data show a strong coupling ($\lambda > 1$) to a non-dispersive E_g phonon mode. The ratio of the dominant E_g phonon mode energy (Ω = 46 meV), to the bare electron bandwidth ($t \approx 800$ meV), places $LiTi_2O_4$in the adiabatic limit ($\Omega/t << 1$) for which the condition $\lambda > 1$ is expected for a small polaron ground state[52]. Second, the observation of the same mode (E_g, oxygen mode) at the Ti-L_3 edge indicates a tightly hybridized state between the localized d^1 titanium electrons and the deformed lattice. Third, we observe large incoherent spectral weight at $E \approx 0.9$ eV, which cannot be accounted for by either of our density-functional perturbation theory (DFPT) or DMFT calculations. We note that polaronic behavior has been previously discussed for $LiTi_2O_4$ based on the anomalous transport behavior of off-stoichiometric samples[53] and previous photoemission and reflectance spectroscopy data[14,54]. Notably, the metallic behavior of $LiTi_2O_4$ at all temperatures contrasts with the localized small Holstein polaron behavior of other titanates[55,56] where a low-temperature insulating state occurs due to reduced lattice mobility. However, in the light regime ($m^* < 10m$), small polarons have been theoretically predicted to be mobile[57,58]. Polaron delocalization involves a crawling-like motion in which an electron is transiently delocalized over two neighboring sites[59], similar to the mechanism suggested here for the $d^{0.5}$ state in $LiTi_2O_4$ (Fig. 4b), in which the dynamical lattice fluctuations are coupled to electron hopping between d^1 and d^0 states. We note that this mobile polaron formation requires an intricate balance between electron–electron correlations and electron-phonon coupling. Dominant electron–electron correlations may choose a charge-ordered ground state[49] while dominant electron-phonon coupling can lead to bi-polaron formation, as suggested for other titanates, like Ti_4O_7[56]. Thus, our data suggests a serendipitous balancing of electron–electron correlations with electron-phonon coupling in this material.

Although $LiTi_2O_4$ has long been thought of as a well-studied BCS superconductor consistent with phonon-dominated superconductivity as in other titanates[46,47], our work forces us to reconsider the notion of conventional superconductivity in $LiTi_2O_4$. Here, a re-examination of $LiTi_2O_4$ using ARPES and RIXS measurements uncovers strong hybridization between titanium and oxygen, considerable electron–electron correlations, and co-existing electron-phonon coupling. In mixed valence $LiTi_2O_4$, this balance of energy scales results in a novel mobile polaronic ground state indicative of a unique balance of charge delocalization, electron–electron correlations, and electron-phonon coupling. $LiTi_2O_4$ becomes a model system to explore predictions of enhancement of superconductivity due to the cooperative effect of electron–electron correlations and electron-phonon coupling in the quarter-filled Hubbard Hamiltonian[60]. Moreover, the proximity of superconductivity to an orbitally ordered phase, the correlated behavior, and the strong hybridization between titanium and oxygen highlight a rich competition between energy scales found only in special classes of quantum materials. Our work expands our understanding of superconductivity in $d^{0.5}$ systems and demonstrates how mixed-valence spinel-oxide structures can host correlated physics, thus broadening our search for material families that can host such correlated phenomena.

Methods

Synthesis of $LiTi_2O_4$ thin films via MBE

We used reactive oxide molecular beam epitaxy (Veeco GEN 10) to synthesize thin film $LiTi_2O_4$ on untreated $MgAl_2O_4$ (111) substrates (CrysTec GmbH). The lithium and titanium fluxes were matched and set to ~1.5×10^{13} atoms/cm^2·s as measured by a quartz crystal microbalance (QCM). We obtained the lithium flux by flowing O_2 during the QCM process and forming Li_2O, as the low atomic mass of elemental lithium yields small frequency changes on the QCM below the detection sensitivity, except for at very high fluxes. For the deposition process, we heated the substrates with a 10.6 μm CO_2 laser to 825 °C in a pressure of $1.0–2.0 \times 10^{-7}$ molecular O_2 over a chamber background pressure of ~5.0×10^{-8}. We co-deposited the lithium and titanium sources for 1 h. After deposition, we shut off the O_2 flow to prevent oxidation of titanium to the 4+ state and cooled at a rate of 100 °C/min.

Structural characterization

Annular dark field (ADF) STEM was performed on Thermofisher Scientific (TFS) Themis (operated at 200 keV, convergence semi-angle 18.9 mrad, ADF collection angle: 36–200 mrad). A small ADF inner collection angle was used to increase light element sensitivity. Electron-transparent TEM samples were prepared using TFS Helios DualBeam FIB/SEM.

Transport measurements

We performed all electrical transport measurements in a Hall bar geometry using evaporated Cr/Au (7 nm/100 nm) contacts with the Hall channel defined by a diamond scribe along the [11-2] crystallographic direction of the $MgAl_2O_4$ (111) substrate. We loaded the samples in 9 T Dynacool Physical Property Measurement System (PPMS) and used AC lock-in techniques at ~15 Hz.

Resonant inelastic X-ray scattering

The XAS and RIXS spectra were collected at the SIX beamline at NSLS-II and the I21 beamline of Diamond Light Source. The Ti L_3-edge was measured at SIX and I21, while the O K-edge spectra were acquired at I21. The Ti L_3-edge energy map is collected at $2\theta = 150°$, while the O K-edge energy map is collected at $2\theta = 90°$. All RIXS spectra are collected at $2\theta = 90°$ at grazing incidence of $\theta = 20°$ unless indicated otherwise. The energy resolution was fixed between 20 to 25 meV at both SIX and Diamond, respectively. All data were measured at a base temperature of 22K at both beamlines.

Angle-resolved photoemission spectroscopy

All in situ photoemission measurements were conducted by immediately transferring the samples through a UHV manifold ($P < 2 \times 10^{-9}$ Torr) to a measurement chamber immediately following film growth. ARPES measurements were taken with a Scienta Omicron DA30-L electron analyzer equipped with a Fermion Instruments BL1200s multi-gas discharge lamp using He-I photons at 21.2 eV, Ne-I photons at 16.85 eV, and He-II photons at 40.2 eV. The base pressure in the ARPES system is maintained during measurements at pressures lower than 5×10^{-11} Torr. ARPES measurements were performed at a temperature of 7K and a nominal experimental energy resolution of 10 meV unless otherwise indicated.

Muon spin relaxation measurements

Low-energy muon spin-relaxation (LE-μSR) measurements were done using the LEM instrument at the Swiss muon source. An applied field of 10 mT was applied transverse to the μ^+s spin polarization direction. For more details on the μSR measurements, refer to Supplementary Material Section S7.

X-ray absorption spectroscopy

XAS of uncapped $LiTi_2O_4$ thin films was performed at 300 K at Beamline 6.3.1 at the Advanced Light Source at Lawrence Berkeley National Laboratory. XAS of capped $LiTi_2O_4$ thin films was performed at 300 K at ID-32 at Diamond Light Source. The spectra from Beamline 6.3.1 represent an average of 4 individual scans. All spectra are taken in the total electron yield configuration. The $LiTi_2O_4$ XAS spectra do not show any polarization dependence. For more details on the XAS, refer to Supplementary Material Section S9.

Data availability

All data used to obtain the conclusions in this paper are presented in the paper and/or the Supplementary Materials. This data may be requested from the authors. Please direct all inquiries to Z.H. (zhasan@g.harvard.edu).

References

1. Matthias, B. T. Chapter V Superconductivity in the Periodic System. *In Progress in Low Temperature Physics*, Vol. 2, 138–150. (C. J. Gorter, ed.) (Elsevier, 1957).
2. Capone, M., Fabrizio, M., Castellani, C. & Tosatti, E. Strongly correlated superconductivity. *Science* **296**, 2364–2366 (2002).
3. Yuan, Z. et al. Correlation-enhanced electron-phonon coupling and superconductivity in (Ba, K)SbO_3 superconductors. *Phys. Rev. B* **105**, 014517 (2022).
4. Nomura, Y., Sakai, S., Capone, M. & Arita, R. Unified understanding of superconductivity and Mott transition in alkali-doped fullerides from first principles. *Sci. Adv.* **1**, e1500568 (2015).
5. Scalapino, D. J. A common thread: the pairing interaction for unconventional superconductors. *Rev. Mod. Phys.* **84**, 1383–1417 (2012).
6. van Loon, E. G. C. P., Rösner, M., Schönhoff, G., Katsnelson, M. I. & Wehling, T. O. Competing coulomb and electron-phonon interactions in NbS_2. *npj Quantum Mater.* **3**, 1–8 (2018).
7. Johnston, D. C. Superconducting and normal state properties of $Li_{1+x}Ti_{2-x}O_4$ spinel compounds. i. preparation, crystallography, superconducting properties, electrical resistivity, dielectric behavior, and magnetic susceptibility. *J. Low. Temp. Phys.* **25**, 145–175 (1976).
8. Wakefield, J. P. et al. Three-dimensional flat bands in pyrochlore metal $CaNi_2$. *Nature* **623**, 301–306 (2023).
9. Sun, C. P. et al. Magnetic field dependence of low-temperature specific heat of the spinel oxide superconductor $LiTi_2O_4$. *Phys. Rev. B* **70**, 054519 (2004).
10. Jin, K. et al. Anomalous magnetoresistance in the spinel superconductor $LiTi_2O_4$. *Nat. Commun.* **6**, 7183 (2015).
11. Wu, W. D. et al. Magnetic penetration depth in V_3Si and $LiTi_2O_4$ measured by μSR. *Hyperfine Interact.* **86**, 615–621 (1994).
12. Okada, Y. et al. Scanning tunnelling spectroscopy of superconductivity on surfaces of $LiTi_2O_4$(111) thin films. *Nat. Commun.* **8**, 15975 (2017).
13. Xue, H. et al. Fourfold symmetric superconductivity in spinel oxide $LiTi_2O_4$(001) thin films. *ACS Nano* **16**, 19464–19471 (2022).
14. Edwards, P. P. et al. A study of the spinel materials $LiTi_2O_4$ and $Li_{43}Ti_{53}O_4$ by photoelectron spectroscopy. *J. Solid State Chem.* **54**, 127–135 (1984).
15. Alexandrov, A. & Ranninger, J. Bipolaronic superconductivity. *Phys. Rev. B* **24**, 1164–1169 (1981).
16. Anderson, P. W. The resonating valence bond state in La_2CuO_4 and superconductivity. *Science* **235**, 1196–1198 (1987).
17. Anderson, P. W., Baskaran, G., Zou, Z. & Hsu, T. Resonating-valence-bond theory of phase transitions and superconductivity in La_2CuO_4-based compounds. *Phys. Rev. Lett.* **58**, 2790–2793 (1987).
18. Oda, T., Shirai, M., Suzuki, N. & Motizuki, K. Electron-phonon interaction, lattice dynamics and superconductivity of an oxide spinel $LiTi_2O_4$. *J. Phys. Condens. Matter* **6**, 6997 (1994).
19. Shen, K. M. et al. Missing quasiparticles and the chemical potential puzzle in the doping evolution of the cuprate superconductors. *Phys. Rev. Lett.* **93**, 267002 (2004).
20. Iwahara, N. & Shikano, S. Vibronic excitations in resonant inelastic x-ray scattering spectra of K_2RuCl_6. *Phys. Rev. Res.* **5**, 023051 (2023).
21. Massidda, S., Yu, J. & Freeman, A. J. Electronic structure and properties of superconducting $LiTi_2O_4$. *Phys. Rev. B* **38**, 11352–11357 (1988).
22. Satpathy, S. & Martin, R. M. Electronic structure of the superconducting oxide spinel $LiTi_2O_4$. *Phys. Rev. B* **36**, 7269–7272 (1987).
23. Li, Q. et al. Evolution of orbital excitations from insulating to superconducting $MgTi_2O_4$ films. *Phys. Rev. B* **107**, L121108 (2023).
24. Bisogni, V. et al. Ground-state oxygen holes and the metal–insulator transition in the negative charge-transfer rare-earth nickelates. *Nat. Commun.* **7**, 13017 (2016).
25. Shi, X. et al. Enhanced superconductivity accompanying a Lifshitz transition in electron-doped FeSe monolayer. *Nat. Commun.* **8**, 14988 (2017).
26. Ohsawa, T. et al. Origin of optical transparency in a transparent superconductor $LiTi_2O_4$. *ACS Appl. Electron. Mater.* **2**, 517–522 (2020).
27. Zhao, M. et al. Pseudo-dielectric functions, band-to-band transitions, and dielectric-related factors in a single-crystal $LiTi_2O_4$ thin film. *Opt. Mater.* **142**, 114034 (2023).
28. Myasnikova, A. E., Zhileeva, E. A. & Moseykin, D. V. Relaxation of strongly coupled electron and phonon fields after photoemission and high-energy part of ARPES spectra of cuprates. *J. Phys. Condens. Matter* **30**, 125601 (2018).
29. Inosov, D. S. et al. Excitation energy map of high-energy dispersion anomalies in cuprates. *Phys. Rev. B Condens. Matter Mater. Phys.* **77**, 212504 (2008).
30. Fujisawa, Y. et al. Imaging emergent exotic quasiparticle states in a frustrated transition metal oxide. Preprint at https://doi.org/10.48550/arXiv.2306.06708(2023).
31. Gilmore, K. et al. Description of resonant inelastic X-ray scattering in correlated metals. *Phys. Rev. X* **11**, 031013 (2021).
32. Green, M. A., Dalton, M., Prassides, K., Day, P. & Neumann, D. A. Lattice vibrations of the superconducting oxide spinels. *J. Phys. Condens. Matter* **9**, 10855–10865 (1997).
33. Heintz, J. M. et al. Superconductivity of $LiTi_2O_4$ and related systems. *Z. Phys. B Condens. Matter* **76**, 303–309 (1989).

34. McCallum, R. W., Johnston, D. C., Luengo, C. A. & Maple, M. B. Superconducting and normal state properties of $Li_{1+x}Ti_{2-x}O_4$ spinel compounds. ii. low-temperature heat capacity. *J. Low. Temp. Phys.* **25**, 177–193 (1976).
35. Kang, M. et al. Holstein polaron in a valley-degenerate two-dimensional semiconductor. *Nat. Mater.* **17**, 676–680 (2018).
36. Hohenadler, M., Aichhorn, M. & Von Der Linden, W. Spectral function of electron-phonon models by cluster perturbation theory. *Phys. Rev. B* **68**, 184304 (2003).
37. Zhou, J. S. et al. Evidence for band renormalizations in strong-coupling superconducting alkali-fulleride films. *Phys. Rev. Lett.* **130**, 216004 (2023).
38. Ament, L. J. P., Van Veenendaal, M. & Van Den Brink, J. Determining the electron-phonon coupling strength from Resonant Inelastic X-ray Scattering at transition metal L-edges. *Europhys. Lett.* **95**, 27008 (2011).
39. Moser, S. et al. Electron-phonon coupling in the bulk of anatase TiO_2 measured by resonant inelastic x-ray spectroscopy. *Phys. Rev. Lett.* **115**, 096404 (2015).
40. Fatale, S., Moser, S., Miyawaki, J., Harada, Y. & Grioni, M. Hybridization and electron-phonon coupling in ferroelectric $BaTiO_3$ probed by resonant inelastic x-ray scattering. *Phys. Rev. B* **94**, 195131 (2016).
41. Braicovich, L. et al. Determining the electron-phonon coupling in superconducting cuprates by resonant inelastic x-ray scattering: methods and results on $Nd_{1+x}Ba_{2-x}Cu_3O_{7-\delta}$. *Phys. Rev. Res.* **2**, 023231 (2020).
42. Abramovitch, D. J., Zhou, J. J., Mravlje, J., Georges, A. & Bernardi, M. Combining electron-phonon and dynamical mean-field theory calculations of correlated materials: transport in the correlated metal Sr_2RuO_4. *Phys. Rev. Mater.* **7**, 093801 (2023).
43. Abramovitch, D. J., Mravlje, J., Zhou, J. J., Georges, A. & Bernardi, M. Respective roles of electron-phonon and electron-electron interactions in the transport and quasiparticle properties of $SrVO_3$. *Phys. Rev. Lett.* **133**, 186501 (2024).
44. He, Y. et al. Rapid change of superconductivity and electron-phonon coupling through critical doping in Bi-2212. *Science* **362**, 62–65 (2018).
45. Wang, Z. et al. Tailoring the nature and strength of electron-phonon interactions in the SrTiO3(001) 2D electron liquid. *Nat. Mater.* **15**, 835–839 (2016).
46. Zhang, C. et al. Enhanced superconductivity in TiO epitaxial thin films. *npj Quantum Mater.* **2**, 1–5 (2017).
47. Yoshimatsu, K., Sakata, O. & Ohtomo, A. Superconductivity in Ti_4O_7 and γ-Ti_3O_5 films. *Sci. Rep.* **7**, 12544 (2017).
48. Popović, Z. V. et al. Phonon properties of the spinel oxide $MgTi_2O_4$ with the S= 1/2 pyrochlore lattice. *Phys. Rev. B* **68**, 224302 (2003).
49. Radaelli, P. G. et al. Formation of isomorphic Ir^{3+} and Ir^{4+} octamers and spin dimerization in the spinel $CuIr_2S_4$. *Nature* **416**, 155–158 (2002).
50. Yang, L. et al. Two-orbital degeneracy lifted local precursor to a metal-insulator transition in $MgTi_2O_4$. *Phys. Rev. B* **102**, 235128 (2020).
51. Kick, M., Grosu, C., Schuderer, M., Scheurer, C. & Oberhofer, H. Mobile small polarons qualitatively explain conductivity in lithium titanium oxide battery electrodes. *J. Phys. Chem. Lett.* **11**, 2535–2540 (2020).
52. Capone, M., Ciuchi, S and Grimaldi, C. The small polaron crossover: role of dimensionality. In *Stripes and Related Phenomena*, 169–174 (Springer, 2000).
53. Watanabe, M., Kaneda, K., Takeda, H. & Tsuda, N. Semiconducting properties of $Li_{1.1}Ti_{1.9}O_4$. *J. Phys. Soc. Jpn.* **53**, 2437–2440 (1984).
54. Harrison, M. R., Edwards, P. P. & Goodenough, J. B. A study of the $Li_{1+x}Ti_{2-x}O_4$ spinel system by diffuse reflectance spectroscopy. *J. Solid State Chem.* **54**, 426–437 (1984).
55. Yang, S., Brant, A. T., Giles, N. C. & Halliburton, L. E. Intrinsic small polarons in rutile TiO_2. *Phys. Rev. B* **87**, 125201 (2013).
56. Lakkis, S., Schlenker, C., Chakraverty, B. K., Buder, R. & Marezio, M. Metal-insulator transitions in Ti_4O_7 single crystals: Crystal characterization, specific heat, and electron paramagnetic resonance. *Phys. Rev. B* **14**, 1429–1440 (1976).
57. Davenport, A. R., Hague, J. P. & Kornilovitch, P. E. Mobile small bipolarons on a three-dimensional cubic lattice. *Phys. Rev. B Condens. Matter Mater. Phys.* **86**, 035106 (2012).
58. Hague, J. P., Kornilovitch, P. E., Samson, J. H. & Alexandrov, A. S. Superlight small bipolarons in the presence of a strong coulomb repulsion. *Phys. Rev. Lett.* **98**, 037002 (2007).
59. Holstein, T. Studies of polaron motion: Part ii. the "small" polaron. *Ann. Phys.* **8**, 343–389 (1959).
60. Clay, R. T. & Roy, D. Superconductivity due to cooperation of electron-electron and electron-phonon interactions at quarter filling. *Phys. Rev. Res.* **2**, 023006 (2020).

Acknowledgements

We thank useful discussions with G. Grissonnanche, M. R. Norman, Y. Wang, F. Baumberger, and J. Sous. This research is primarily supported by the National Science Foundation, Division of Materials Research, under Award No. DMR-2339913. Materials growth and photoemission studies were supported by the Platform for the Accelerated Realization, Analysis, and Discovery of Interface Materials (PARADIM) under NSF Cooperative Agreement No. DMR-2039380. All nanofabrication work was performed at Harvard University's Center for Nanoscale Systems (CNS), a member of the National Nanotechnology Coordinated Infrastructure Network (NNCI), supported by the National Science Foundation under NSF Grant No. 2025158. Z.H. and G.A.P. acknowledge support from the Paul & Daisy Soros Fellowship for New Americans. G.A.P. acknowledges additional support from the NSF Graduate Research Fellowship Grant No. DGE-1745303. A.K. and K.C.N. acknowledge support from the Air Force Research Laboratory, Project Grant FA95502110429. S.H.S. and I.E.B. acknowledge support from the Rowland Institute at Harvard University. J.A.M. acknowledges support from the Packard Foundation and the Sloan Foundation. This research used beamline 2-ID of the National Synchrotron Light Source II, which is a US DOE Office of Science Facility operated for the DOE Office of Science by Brookhaven National Laboratory under contract no. DE-SC0012704. HL and ASB acknowledge support from NSF Grant No. DMR-2323971. The μSR experiments were performed at the Swiss Muon Source, SμS, Paul Scherrer Institute, Villigen, Switzerland. Certain commercial equipment, instruments, software, or materials are identified in this paper in order to specify the experimental procedure adequately. Such identifications are not intended to imply recommendation or endorsement by NIST, nor are they intended to imply that the materials or equipment identified are necessarily the best available for the purpose. This research used resources of the Advanced Light Source, which is a DOE Office of Science User Facility under contract no. DE-AC02-05CH11231.

Author contributions

Z.H., G.A.P., C.M.B., and J.A.M. synthesized the thin films with assistance from M.R.B. and D.G.S. Electrical transport measurements were performed and analyzed by G.A.P. Scanning transmission electron microscopy was performed by S.H.S. and I.E. ARPES measurements were performed by Z.H., G.A.P., and B.D.F. ARPES analysis was done by Z.H. and B.D.F. with support from A.d.l.T. The RIXS measurements were performed by Z.H., E.M., S.H.S., I.B., and A.d.l.T. with support from V.B., J.P., M.G.F., and K.Z. RIXS analysis was done by Z.H., S.H.S., and E.M under the supervision of A.d.l.T. XAS measurements were supported by A.T.N. μSR measurements were performed by A.J.G. and P.P.B. with support from A.S., Z.S., and T.P. Analysis of μSR data was done by A.J.G. and P.P.B. Scanning SQUID measurements were performed by A.K. and K.C.N. H.L., S.S., and A.S.B. performed the DFT, DMFT, and electron-

phonon calculations. J.A.M. and A.d.l.T. conceived and guided the study. Z.H., G.A.P., J.A.M., and A.d.l.T. wrote the manuscript with contributions and discussion from all authors.

Competing interests
The authors declare no competing interests.

Additional information
Supplementary information The online version contains supplementary material available at https://doi.org/10.1038/s41467-025-68068-7.

Correspondence and requests for materials should be addressed to Alberto de la Torre or Julia A. Mundy.

Peer review information *Nature Communications* thanks the anonymous reviewers for their contribution to the peer review of this work. A peer review file is available.

Reprints and permissions information is available at http://www.nature.com/reprints

Publisher's note Springer Nature remains neutral with regard to jurisdictional claims in published maps and institutional affiliations.

[1]Department of Physics, Harvard University, Cambridge, MA, USA. [2]Department of Physics, Arizona State University, Tempe, AZ, USA. [3]Laboratory of Atomic and Solid-State Physics, Cornell University, Ithaca, NY, USA. [4]The Rowland Institute, Harvard University, Cambridge, MA, USA. [5]NIST Center for Neutron Research, National Institute for Standards and Technology, Gaithersburg, MD, USA. [6]Department of Physics, Northeastern University, Boston, MA, USA. [7]Quantum Materials and Sensing Institute, Northeastern University, Burlington, MA, USA. [8]National Synchrotron Light Source II, Brookhaven National Laboratory, Upton, NY, USA. [9]Advanced Light Source, Lawrence Berkeley National Laboratory, Berkeley, CA, USA. [10]PSI Center for Neutron and Muon Sciences, Villigen, Switzerland. [11]Diamond Light Source, Harwell Campus, Didcot, UK. [12]Platform for the Accelerated Realization, Analysis, and Discovery of Interface Materials (PARADIM), Cornell University, Ithaca, NY, USA. [13]Department of Materials Science and Engineering, Cornell University, Ithaca, NY, USA. [14]Kavli Institute at Cornell for Nanoscale Science, Ithaca, NY, USA. [15]Leibniz-Institut für Kristallzüchtung, Berlin, Germany. [16]These authors contributed equally: Zubia Hasan, Grace A. Pan. ✉e-mail: a.delatorreduran@northeastern.edu; mundy@fas.harvard.edu